Phase-contrast imaging and tomography at 60 keV using a conventional x-ray tube source

Tilman Donath,[1,a)] Franz Pfeiffer,[1,2,b)] Oliver Bunk,[1] Waldemar Groot,[1] Martin Bednarzik,[1] Christian Grünzweig,[1] Eckhard Hempel,[3] Stefan Popescu,[3] Martin Hoheisel,[3] and Christian David[1]
[1]*Paul Scherrer Institut, 5232 Villigen PSI, Switzerland*
[2]*Ecole Polytechnique Fédérale de Lausanne, 1015 Lausanne, Switzerland*
[3]*Siemens AG, Healthcare Sector, 91301 Forchheim, Germany*

(Received 19 January 2009; accepted 13 April 2009; published online 11 May 2009)

Phase-contrast imaging at laboratory-based x-ray sources using grating interferometers has been developed over the last few years for x-ray energies of up to 28 keV. Here, we show first phase-contrast projection and tomographic images recorded at significantly higher x-ray energies, produced by an x-ray tube source operated at 100 kV acceleration voltage. We find our measured tomographic phase images in good agreement with tabulated data. The extension of phase-contrast imaging to this significantly higher x-ray energy opens up many applications of the technique in medicine and industrial nondestructive testing. © *2009 American Institute of Physics.*
[DOI: 10.1063/1.3127712]

I. INTRODUCTION

The contrast in conventional x-ray radiography and computed tomography (CT) arises from the attenuation of x rays (by absorption or scatter processes) in the examined object. Phase-sensitive x-ray imaging, which uses the phase shift rather than the absorption as the imaging signal, has the potential of substantially increased contrast in biological samples.[1–4] Differential phase-contrast radiography and tomography have been developed over the last few years[5–12] and allows for the simultaneous measurement of the conventional attenuation signal and an additional phase signal, within a single measurement. The method was first demonstrated at synchrotron-radiation x-ray sources using an intense and almost parallel x-ray beam with a narrow wavelength spectrum.[5–7,10] Shortly after these initial high-brilliance applications, this phase-contrast method was implemented with conventional low-brilliance x-ray tube sources.[8,9,11,12] So far, the x-ray grating interferometer has been used up to x-ray energies of 28 keV.

However, for most clinical and industrial nondestructive testing applications, an even higher x-ray energy is required. The major difficulty for the grating interferometer to function at higher x-ray energies is imposed by the microfabricational challenges of producing periodic one-dimensional gratings with structures that are sufficiently high to result in enough contrast for the image formation process.

II. MATERIALS AND METHODS

A. Differential phase-contrast projections

The scheme in Fig. 1 shows the principle of projection imaging with a grating interferometer. Here, in contrast to conventional radiography, not only the intensity of x-rays but also their deflection angle is determined. Figure 1(a) schematically shows the deflection of x rays penetrating a cylindrical object.

For the conventional radiography image, the attenuation (or transmission) signal is determined from the intensity I of the x-ray beam that has penetrated the sample and the (reference) intensity I_0 measured without the sample in the beam. From these measurements, the projection

$$p(t,z) = -\ln\frac{I(t,z)}{I_0(t,z)} = \int ds\,\mu(x,y,z) \tag{1}$$

is calculated. The right hand side of this equation describes the projection of the linear attenuation coefficient $\mu(x,y,z)$ along the x-ray path s. The additional phase signal is simply the deflection angle, i.e., the angle between the reference beam without the sample and the transmitted x-ray beam, when the sample is inserted. The deflection is approximately given by

$$\alpha(t,z) = \frac{\partial}{\partial t}\int ds\,\delta(x,y,z), \tag{2}$$

where

$$n = 1 - \delta(x,y,z) + i\beta(x,y,z) \tag{3}$$

is the complex refractive index of the sample. Here, the imaginary part β of the refractive index describes the attenuation of x rays and is related to the linear attenuation coefficient μ as $\beta = \mu\lambda/4\pi$ for x-ray wavelength λ, while the real part δ, which is called the refractive index decrement, determines the phase shift and the deflection angle caused by the sample. The direction of the partial derivative in Eq. (2) is perpendicular to the grating structures and explains the differential nature of the (differential) phase-contrast images.

[a)]Electronic mail: tilman.donath@psi.ch.
[b)]Present address: Physik-Department (E17), Technische Universität München, 85748 Garching, Germany.

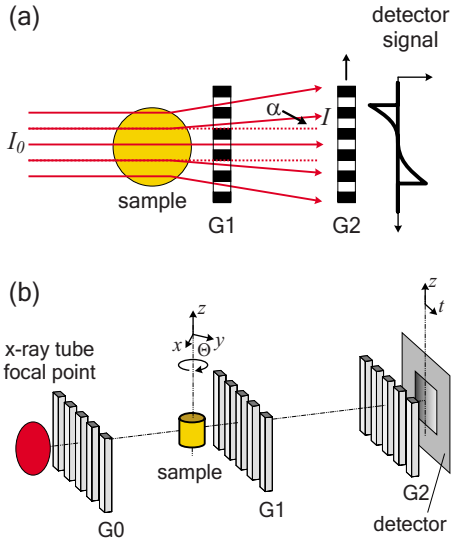

FIG. 1. (Color online) Phase-contrast measurement using a grating interferometer. (a) The beam deflection caused by the sample is transformed into an intensity variation that is detected with a conventional two-dimensional x-ray detector. During a phase-stepping scan, grating G2 is moved stepwise perpendicular to the grating structures, while the intensity oscillation is recorded for each detector pixel. (b) Arrangement of the symmetric grating interferometer using a conventional x-ray tube source. The interferometer consists of two absorption gratings G0 and G2 and one phase grating G1.

B. Projections from phase scans

The grating interferometer allows measuring intensity and propagation directions of the x-ray beam simultaneously and independently for each detector pixel. Due to the Talbot effect, the grating structure of G1 is reproduced as an interference pattern in the plane of G2. G2 has the same periodicity as the interference pattern. The relative position of the interference pattern and the G2 grating determines the amount of x-ray intensity that is transmitted through G2. This allows determining of the relative position in a so-called phase-stepping scan, in which the intensity oscillation is recorded for each detector pixel, while the G2 grating is stepped by an integer number of steps over a distance corresponding to one or several times its period p_2. From the recorded phase-stepping scan, both the transmitted intensity and the deflection angle are calculated. The transmitted intensity is simply given by the average of all data points, while the relative position of interference pattern and G2 is deduced from the phase of the first Fourier component of a discrete Fourier transform of the recorded oscillation for each pixel. The change in this phase determines the deflection angle caused by introduction of the sample. Thus, the conventional attenuation signal and the phase signal are simultaneously obtained from a single phase-stepping scan.

C. Tomographic reconstruction

In conventional tomography, two-dimensional projection images $p_\theta(t,z)$ are recorded for many different projection angles θ and used to reconstruct the three-dimensional distribution of the attenuation coefficient $\mu(x,y,z)$ inside the sample. From the phase-contrast projections $\alpha(t,z)$ one additionally reconstructs the distribution of the refractive index decrement $\delta(x,y,z)$ inside the sample. In the reconstruction of the phase-contrast projections, however, we have to consider the differential nature of these projections. Applying a modified filtered-backprojection algorithm for the reconstruction, with an imaginary sign (f) frequency filter (Hilbert filter) instead of the usual ramp-function frequency filter $|f|$, correctly accounts for this behavior.[11,13] Together, the reconstructed signals $\delta(x,y,z)$ and $\mu(x,y,z)$ describe the entire complex refractive index distribution given in Eq. (3).

TABLE I. Parameters of the constructed symmetric grating interferometer for 60 keV.

Geometrical and grating parameters	
G0-G1 distance	875 mm
G1-G2 distance	875 mm
Talbot order	First
Absorption gratings G0 and G2	Au, $p_0=p_2=8.5$ μm, $h_0=h_2=90$ μm
Phase grating G1 (pi-shifting)	Si, $p_1=8.5$ μm, $h_1=75$ μm

D. Grating-interferometer setup for 60 keV

Our grating interferometer is designed for the operation with x-ray tube sources and consists of three gratings, as shown in Fig. 1(b). G1 is a π-phase-shifting phase grating. The propagation of G1 results in a periodic intensity distribution in the plane of G2 with the same frequency as G2. Grating G2 is an absorbing grating positioned in the first fractional Talbot plane behind G1, and grating G0 is an absorbing grating that maintains the spatial coherence properties even for the extended source point of an x-ray tube. All gratings, i.e., the absorption gratings G0, G2, and the phase grating G1, were produced with the same period of $p_0=p_1=p_2=8.5$ μm. The equal periods result in a symmetric grating geometry, in which the G0-to-G1 and G1-to-G2 distances are equal as can easily be deduced from the Talbot imaging formulas given by Weitkamp *et al.*[9] Hence, we refer to this geometry as a symmetric grating interferometer. The current design with equal period of all gratings reduced the grating production time, since G0 and G2 could be manufactured within the same process.

The gratings were produced on 100 mm silicon wafers using photolithography, wet etching into silicon, and electroplating of gold.[14] They were placed with their lines perpendicular to the optical axis of the interferometer and parallel to the axis of tomographic rotation as shown in Fig. 1. The G1 grating was produced in silicon with a structure height of $h_1=75$ μm, which is the Si thickness that produces a phase shift of one-half wavelength at a photon energy of 60 keV, for which the interferometer was designed. The G0 and G2 gratings were produced using a frequency-doubling technique,[14] in which a silicon structure of the double period was covered with a gold structure of height $h_0=h_2=90$ μm. The parameters of our grating interferometer are summarized in Table I.

The grating interferometer is operated within a conventional radiography setup consisting of x-ray tube and x-ray camera. The x-ray tube in our setup is a MXR-160HP/11 of Comet AG, a water-cooled fixed anode tube with a tungsten target, and a target angle of 11°. For the measurements pre-

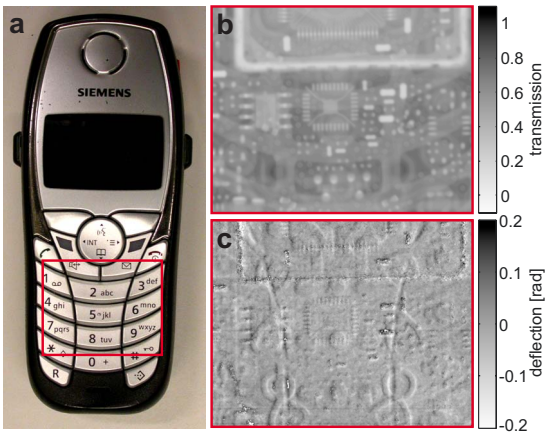

FIG. 2. (Color online) Phase-contrast projections of a mobile phone. (a) Photograph with a rectangular box showing the location of (b) the conventional transmission image and (c) the phase-contrast image. The phase-contrast image shows the deflection angle in units of the phase shift of the oscillation in the phase-stepping scan.

sented here, the tube was operated at 100 kV, 10 mA, and with an effective source point of 1 mm diameter. The beam was prefiltered by 30 mm of aluminum. The resulting x-ray spectrum had a mean photon energy of about 65 keV. The x-ray camera in our setup is a self-built device based on lens-coupled imaging of a luminescent screen. It consists of a CsI scintillator of Hamamatsu (columnar growth CsI with a structure height of 600 μm) that converts the x rays into visible light. The visible light image is projected over a 90°-deflecting mirror and an objective lens onto a charge-coupled device (CCD) camera (Proline of Finger Lakes Instrumentation) with 1024×1024 pixels (Ref. 15) corresponding to a field of view of 65×65 mm^2.

III. EXPERIMENTS AND RESULTS

The grating interferometer for 60 keV was built and tested at the Laboratory for Micro- and Nanotechnology at the Paul Scherrer Institut. After the first alignment of the interferometer, we measured a fringe visibility of 3%. Here the visibility was calculated as the ratio of the amplitude to the mean value of the intensity oscillation in the phase-stepping scan. This measured visibility was significantly lower than the value of 8% predicted by simulations for the given design parameters. The deviation was most likely due to imperfections in the first set of microstructured gratings that we used. By now, the gratings were replaced with a second set of gratings, whereby the visibility could be increased to about 8%. However, the first set of gratings with only 3% visibility was used to record the projection and CT images that are presented here.

Measured projection images of a portable phone are shown in Fig. 2. Figure 2(b) shows the conventional transmission image and Fig. 2(c) shows the phase-contrast image. Both images were derived from the same phase-stepping data, with 16 phase steps recorded over one period of G2. The data were recorded at an x-ray tube setting of 100 kV, 10 mA with 3 s exposure per phase step. The projection images show a region of 451×357 pixels (at binning factor of 2), which correspond to an area of 28.7×22.7 mm^2 at the sample position. One can immediately recognize the different nature of the conventional image [Fig. 2(b)] and the phase-contrast image [Fig. 2(c)]. The phase-contrast image shows the directional derivative (from left to right) of the phase projection as described by Eq. (2). Thus, vertical edges appear more pronounced in the phase image. Besides this difference, we find that different structures become visible in both images. While the conventional image clearly shows the strongly absorbing metal parts, other details are more clearly visible in the phase-contrast image. They seem to be related mainly to the structure in the plastic cover of the phone.

We also performed a tomography scan on a simple test phantom. The phantom was a polymethyl methacrylate (PMMA) cylinder with a diameter of 30 mm and with the text "PSI" (abbreviation for "Paul Scherrer Institut") milled into it on a CNC machine. Actually, two identical cylinders with different texts were attached to each other using sticky tape and scanned simultaneously. The bottom cylinder was glued to a sample holder from aluminum. We recorded 361 projections of 511×362 pixels and applied the appropriate filtered-backprojection algorithms for the reconstruction of the conventional and the phase data as described above, the reconstructed volume measuring $511\times511\times362$ voxels. Cross sections and a volume rendering are shown in Figs. 3(a) and 3(b) for the reconstruction of the conventional and the phase data, respectively. The sticky tape is visible in the conventional reconstruction as a tiny bright ring around the cylinders. The thickest part of the ring is found above the left side of the letter "P" were two tape layers overlap. It is also visible in the phase images but with almost no contrast. Eventually, high Z-elements in the sticky tape give rise to the strong observed attenuation contrast in the conventional image. Sample holder and glue are visible at the bottom of the longitudinal cross sections.

In order to verify correct operation of the grating interferometer at the design energy, we determined the effective x-ray energy at which the phase measurement was performed. The effective x-ray energy of the measurement was deduced by comparing the measured refractive index decrement of PMMA obtained from the phase reconstruction with the theoretically expected $\delta_{\mathrm{th}}(E)$ as a function of x-ray energy E. For the calculation of $\delta_{\mathrm{th}}(E)$ we used tabulated data of Kissel.[16] We determined mean value and standard deviation of the reconstructed $\delta(x,y,z)$ from one pixel over $N=21$ adjacent reconstructed slices. The obtained refractive index decrement and standard deviation of $\delta=(7.1\pm0.2)\times10^{-8}$ for PMMA correspond to the theoretical value at $E=(61.2\pm0.8)$ keV x-ray energy. Thus, our phase measurement was conducted with an effective x-ray energy of 61.2 keV that deviates by only 2% from the design value. This measured effective energy is a result of the x-ray spectrum, the spectral efficiency of the x-ray camera, and the spectral efficiency of the grating interferometer.

IV. SUMMARY AND CONCLUSIONS

In summary, we have constructed and experimentally validated the first x-ray grating interferometer for 60 keV mean x-ray energy. Thereby, we have more than doubled the

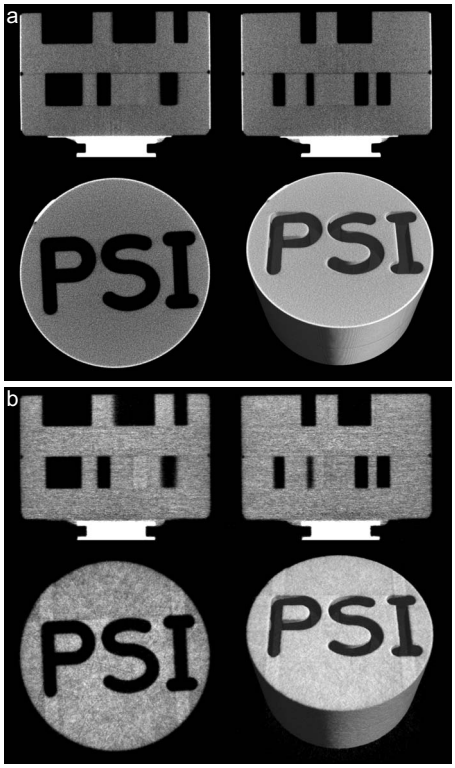

FIG. 3. CT reconstructions of a PMMA phantom. Shown are the (a) conventional reconstruction and (b) the phase-contrast reconstruction. The phantom consists of two PMMA cylinders of 30 mm diameter. The text PSI was milled into the upper cylinder on a CNC machine. Contrast is obtained between the air-filled letters and PMMA. Both images show cross sections for three orthogonal directions, the reconstructed slice (bottom left) and two longitudinal cross sections (top left, top right), as well as a 3D rendering (bottom right). The sticky tape used to attach the two cylinders to each other is visible in the conventional reconstruction as a small bright ring around the cylinder. The thickest part of the ring is found above the left side of the letter P where two tape layers overlap. The bottom cylinder was glued to a sample holder from aluminum. Sample holder and glue are visible at the bottom of the longitudinal cross sections.

x-ray energy range that is accessible for x-ray phase-contrast imaging. We could confirm that our tomographic measurements indeed result in a measurement of the refractive index decrement that corresponds to the literature values for the effective x-ray energy of 61.2 keV. The extension of phase-contrast imaging from the so far achieved 28 keV to the here achieved more than 60 keV enables the investigation of significantly larger samples now. As example, the 10% transmission thicknesses for water, aluminum, and iron are given in Table II. Increasing the x-ray energy from 28 to 60 keV, the transmission thickness of water is almost doubled from 57.3 to 112.6 mm (ratio of 1.97). The relative increase for aluminum (4.80) and iron (8.36) is even bigger because of the higher Z-number of these elements. The accessible transmission thickness of more than 100 mm in water or waterlike body tissues makes phase-contrast CT in clinical applications possible. Thus, the extension to this higher energy opens up applications of the technique in medicine and industrial nondestructive testing.

TABLE II. Material thickness with 10% transmission remaining for selected materials at 28 and 60 keV. The relative increase in the transmission thickness going from 28 to 60 keV is given by the ratio column.

	10% transmission thickness (mm)		
Material	At 28 keV	At 60 keV	Ratio
Water (H2O)	57.3	112.6	1.97
Aluminum (Al)	6.5	31.0	4.80
Iron (Fe)	0.30	2.5	8.36

[1] J. Clauser, U.S. Patent No. 5,812,629 (22 September 1998).
[2] A. Momose, Opt. Express **11**, 2303 (2003).
[3] A. Momose, Jpn. J. Appl. Phys., Part 1 **44**, 6355 (2005).
[4] S.-A. Zhou and A. Brahme, Phys. Medica **24**, 129 (2008).
[5] A. Momose, S. Kawamoto, I. Koyama, Y. Hamaishi, K. Takai, and Y. Suzuki, Jpn. J. Appl. Phys., Part 2 **42**, L866 (2003).
[6] T. Weitkamp, A. Diaz, C. David, F. Pfeiffer, M. Stampanoni, P. Cloetens, and E. Ziegler, Opt. Express **13**, 6296 (2005).
[7] A. Momose, W. Yashiro, Y. Takeda, Y. Suzuki, and T. Hattori, Jpn. J. Appl. Phys., Part 1 **45**, 5254 (2006).
[8] F. Pfeiffer, T. Weitkamp, O. Bunk, and C. David, Nat. Phys. **2**, 258 (2006).
[9] T. Weitkamp, C. David, C. Kottler, O. Bunk, and F. Pfeiffer, Proc. SPIE **6318**, 63180S (2006).
[10] F. Pfeiffer, O. Bunk, C. David, M. Bech, G. Le Duc, A. Bravin, and P. Cloetens, Phys. Med. Biol. **52**, 6923 (2007).
[11] F. Pfeiffer, C. Kottler, O. Bunk, and C. David, Phys. Rev. Lett. **98**, 108105 (2007).
[12] F. Pfeiffer, O. Bunk, C. Kottler, and C. David, Nucl. Instrum. Methods Phys. Res. A **580**, 925 (2007).
[13] G. W. Faris and R. L. Byer, Appl. Opt. **27**, 5202 (1988).
[14] C. David, J. Bruder, T. Rohbeck, C. Grünzweig, C. Kottler, A. Diaz, O. Bunk, and F. Pfeiffer, Microelectron. Eng. **84**, 1172 (2007).
[15] The camera was operated in binning mode, with a binning factor of 2, in order to match the effective pixel size to the spatial resolution in our imaging geometry and to speed up the measurements.
[16] We calculated $\delta_{th}(E)$ from the tabulated data by L. Kissel for elastic photon-atom scattering, anomalous scattering factors as given by the file f1f2_asf_Kissel.dat of the DABAX library. See http://ftp.esrf.eu/pub/scisoft/xop2.3/DabaxFiles/.